Kelvin-Helmholtz-like instability of phospholipid bilayers under shear flow: System-size dependence

Taiki Shigematsu [1,*] Kenichiro Koshiyama [2] and Shigeo Wada [1]

[1]*Department of Mechanical Science and Bioengineering, Graduate School of Engineering Science, Osaka University, Toyonaka, Osaka, 560-8531, Japan*
[2]*Graduate School of Technology, Industrial and Social Sciences, Tokushima University, Tokushima 770-8506, Japan*

We performed a series of molecular dynamics (MD) simulations of phospholipid bilayers under shear flow to estimate the effect of the system size on Kelvin-Helmholtz (KH)-like instability of the bilayer at the molecular scale. To extend the estimation by the MD simulations to the microscale, we introduced linear stability analysis for the fluid–fluid interface consisting of a thin membrane. For both the MD simulations and theoretical model, the critical velocity difference across the bilayer, where instability occurs, decreased with increasing wavelength of the bilayer undulation λ, which corresponds to the system size. When λ was more than about ten times larger than the bilayer thickness, the critical velocity difference in the MD simulations was in quantitative agreement with that obtained by the theoretical model. This means that the theoretical model is applicable for the shear-induced KH-like instability of the bilayer for large λ. The theoretical model showed that the critical velocity difference for the KH-like instability was proportional to $\lambda^{-3/2}$. Based on these results, we discuss the implications of the shear-induced bilayer instability in the shear-induced cell damage observed in experiments.

I. INTRODUCTION

Biological cells are known to respond to surrounding flow fields and change their activities in the physiological environment [1–3]. In contrast, the nonphysiological high shear flow generated by medical devices or treatment techniques, such as ventricular-assisted devices [4], jet injectors [5], and sonoporation treatment [6,7], can induce rupture of the cell membrane and subsequent cell death. For the development of such devices, it is essential to understand the mechanism of membrane rupture and control it under shear flow. However, because the details of membrane rupture are elusive in experiments, the mechanism of membrane rupture is not fully understood.

Many experiments and numerical simulations of biological cells or the vesicles of phospholipid bilayers, which are the fundamental structure of the cell membrane and used as a model cell membrane, under shear flow have been performed [8–10]. These studies showed that the cells (e.g., red blood cells) were elongated under shear flow and the membrane tension increased with increasing shear rate. When the tension exceeded the limit of the membrane, membrane rupture may occur. This cell-elongation-induced rupture was believed to be a common mechanism of membrane rupture under shear flow. Hanasaki and co-workers [11] performed molecular dynamics (MD) simulations of the phospholipid bilayer under shear flow. They found that buckling-like and/or Kelvin-Helmholtz (KH)-like instabilities of the bilayer occurred and resulted in bilayer rupture when the applied shear rate exceeded a critical value. They also found that the instability pattern

and the critical shear rate varied depending on the size and the aspect ratio of the bilayer system at the molecular scale. Although the buckling-like instability has been investigated especially for a lamellar phase of bilayer membranes, i.e., onion formation [12–15], little is known about the KH-like instability and especially its critical value at the larger scale (microscale). Estimating the effect of the system size on the KH-like instability beyond the molecular scale will facilitate discussion whether the KH-like instability is observable in the microscopic experiments.

Although molecular-scale imaging techniques have advanced year by year, molecular-scale dynamical phenomena are still elusive. MD simulation is a powerful tool to numerically observe molecular-scale dynamical phenomena. Many researchers investigated the dynamical phenomena of the phospholipid bilayer under mechanical stresses, including the shear-induced instability [11], formation of transmembrane pores [16], and phase transition [17]. They found that the critical stress level (i.e., the shear rate, tension, or strain) for inducing such dynamical phenomena varies depending on the system size. However, in MD simulations, the wavelengths of the phenomena are limited within the simulation box (< 100 nm) and far from those in experiments. Therefore, it is challenging to quantitatively estimate the critical values in experiments based only on MD simulation results.

To bridge the gap between MD simulations and experiments, various theoretical models have been proposed. For example, Tolepkina and co-workers [16] proposed a free energy model of the stretched bilayer to explain the order of magnitude difference between the critical values of pore formation. Shigematsu and co-workers [17] proposed a free energy model to explain the stretch-induced phase transition of a bilayer. However, for the
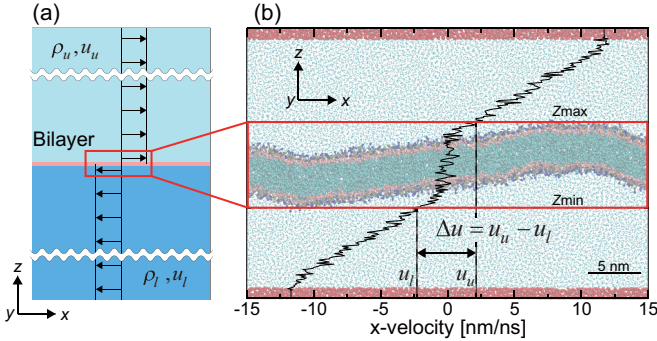
*shigematsu@bpe.es.osaka-u.ac.jp

FIG. 1. (a) Schematic of the theoretical situation in which a water bath is divided by a thin phospholipid bilayer. (b) Representative velocity profile of the S6x1 system overlaid on its snapshot. The definition of the velocity difference Δu_{MD} is also shown. The choline, phosphate, glycerol, and hydrocarbon particles of the DPPC molecules are shown in blue, tan, pink, and cyan, respectively. The water and wall particles are shown in light blue and red, respectively.

shear-induced KH-like instability of the bilayer, such a theoretical approach has, to our knowledge, not been performed and the existence of the instability in experiments is still under discussion.

The objective of this study is to estimate the effect of the system size on the shear-induced KH-like instability of the phospholipid bilayer not only at the molecular scale, but also at the microscale. To achieve this objective, we performed MD simulations of phospholipid bilayers under shear flow. Additionally, we modeled the bilayer as a thin membrane at a fluid–fluid interface and evaluated its stability under the framework of linear stability analysis [18]. By using this framework, estimation of the system size dependence at the molecular scale in the MD simulation can be extended to the microscale. Based on these results, we discuss the implications of the shear-induced bilayer instability in the shear-induced cell damage observed in experiments.

The remainder of the paper is organized as follows. In Sec. II, we describe the details of the theoretical model used in the linear stability analysis and obtain the stability criterion of the bilayer under shear flow. In Sec. III, we describe the MD simulation methods used for the bilayer under shear flow. In Sec. IV, we present the MD simulation results of the threshold of the shear-induced KH-like instability and discuss the consistency of the instability between the model and simulation. Finally, the conclusions are provided in Sec. V.

II. THEORY

Let us consider a water bath divided by a phospholipid bilayer on the x-y plane [see Fig. 1(a)]. The bilayer is symmetric between the upper and lower layers, and it is sufficiently thin so that its thickness can be ignored. We assume uniform displacement along the y direction and also assume water as the incompressible inviscid fluid. The velocity and density of water are assumed to discontinuously change across the bilayer. This indicates the complete slip condition at the bilayer, although slipping of water on the

bilayer did not completely occur in the MD simulations [see Fig. 1(b)].

For the deformation energy of the bilayer, we use the Helfrich Hamiltonian F [19]. The Hamiltonian is a curvature elastic energy model of fluid membranes with negligibly small thickness

$$F = \int \left\{ \sigma + \frac{1}{2} k_c (c_1 + c_2 - c_0)^2 \right\} dA, \qquad (1)$$

where σ and k_c are the tension and bending modulus of the bilayer, respectively. c_1 and c_2 are the principal curvatures and c_0 is the spontaneous curvature. Owing to the symmetric bilayer, c_0 can be considered to be 0. dA is the surface element. To properly apply this Hamiltonian to a bilayer, the bilayer size should be more than about ten times larger than the thickness of the hydrophobic part of the bilayer so that the assumption of the negligibly small thickness is valid [20]. Through conventional linear stability analysis of the small undulation of the bilayer with F, we can obtain the stability criterion [21]

$$|\Delta u| < \sqrt{\frac{\rho_u + \rho_l}{\rho_u \rho_l} \left\{ k_c \left(\frac{2\pi}{\lambda} \right)^3 + \sigma \frac{2\pi}{\lambda} - \frac{\rho_u - \rho_l}{g} \left(\frac{\lambda}{2\pi} \right) \right\}}, \qquad (2)$$

where λ is the wavelength of bilayer undulation, g is gravitational acceleration, ρ_u and ρ_l are the water densities in the upper and lower regions, respectively, and Δu is the velocity difference across the bilayer. We assume that there is no density difference ($\rho = \rho_u = \rho_l$) and that the surface tension is zero even under shear flow. It is noted that there is a possibility that shear flow generates a force suppressing the bilayer undulation and induces an effective tension of the bilayer [14,15]. Although these shear-induced force and tension were ignored in this paper, considering them may improve the model prediction. Under these assumptions, Eq. (2) can be rearranged as

$$|\Delta u| < \sqrt{\frac{16\pi^3 k_c}{\rho \lambda^3}}. \qquad (3)$$

This equation provides the limit of the stable bilayer depending on the undulation wavelength λ. After the water density ρ and bending modulus of the bilayer k_c are obtained, we can estimate the critical velocity difference $|\Delta u_c|$, which induces instability of the bilayer, with respect to the wavelength of bilayer undulation λ.

III. METHOD

A. System

We used four dipalmitoylphosphatidylcholine (DPPC) bilayer systems containing different numbers of DPPC molecules. To model the molecules, we used the MARTINI force field [22], which is a coarse-grained model suitable for semi-quantitative evaluation of lipid dynamics. The base bilayer system was constructed using the Martini Bilayer Maker of CHARMM-GUI [23]. The base system was composed of 128 DPPC molecules and 7000 water beads in a rectangular simulation box with periodic boundary conditions, in which the bilayer was placed on the x-y plane and each of the

leaflets of the bilayer was composed of the same number of DPPC molecules. The base system was equilibrated by a MD simulation under constant temperature (323 K) and pressure (0.1 MPa). After equilibration, the system box size (l_x, l_y, l_z) was $6.3 \times 6.3 \times 25.2$ nm^3 and the thickness of the hydrophobic part of the bilayer was about 3 nm. The base bilayer system was replicated 2, 6, 8, and 12 times in the x direction, and the replicated bilayer systems are called S2x1, S6x1, S8x1, and S12x1, respectively. As the systems with small l_y suppress the buckling-like instability along the y direction, we can focus on the KH-like instability [11]. These systems were equilibrated by MD simulations under constant temperature (323 K), constant pressure in the x and z directions (0.1 MPa), and constant length of the simulation box in the y direction for at least 1.2 μs.

The parameter settings of the MD simulations were taken from a previous study about the MARTINI force field [24]. The van der Waals and Coulomb interactions were smoothly shifted to 0 between 0.9 and 1.2 nm and between 0.0 and 1.2 nm, respectively, by using the GROMACS shift function. The neighbor list with a cutoff of 1.2 nm was updated every ten steps. The temperature and pressure were maintained by the Berendsen weak coupling method [25] with 2.0 and 4.0 ps time constants, respectively. To numerically solve the equations of motion, we used the leap-frog algorithm with a time step 40 fs. All of the MD calculations were performed with GROMACS 5.1 [26,27], and all of the snapshots of the bilayer system were produced with VISUAL MOLECULAR DYNAMICS [28].

B. Shear-flow simulation

The bilayer under shear flow was expressed by a similar method to that proposed by Hanasaki and co-workers [11]. In the shear-flow simulation, the systems were divided into bins in the z direction. The z width of each bin was about 1.0 nm. At the beginning of the shear-flow simulation, the water beads in both the top and bottom bins were defined as wall particles [see the red part of Fig. 1(b)]. During the shear-flow simulation, their velocities were set to constant values of $(V_x, 0, 0)$ and $(-V_x, 0, 0)$ for the top and bottom bins, respectively, regardless of the forces from other particles. The parallel walls moving with different constant velocities generated shear flow in between the walls. The force field parameters of the wall particles were the same as those of the water beads, but the interactions between the wall particles were ignored to avoid friction between the top and bottom walls across the periodic boundary in the z direction. To maintain the temperature of the system under shear flow, the temperatures of the molecules in the bins were separately kept at 323 K by the Berendsen weak coupling method [25] with a 2.0-ps time constant. During the shear-flow simulation, the system box size was constant. The shear rate $\dot{\gamma}$ is defined as $\dot{\gamma} = 2V_x/l_m$, where l_m is the distance between the top and bottom walls in the z direction. To locally apply the Berendsen weak coupling method, we modified the original source code of GROMACS 5.1 [26,27]. Verification of this modification and effects of the local temperature control on the local structure of water are given in Appendixes A and B, respectively.

An initial configuration was taken from the final 800 ns of the trajectory of the equilibration simulation of each bilayer system. To suppress the disturbance after switching the simulation conditions of the equilibration simulation to those of the shear-flow simulation, a pre-shear-flow simulation was performed with $\dot{\gamma} = 0$ for 600 ns. Ten different configurations were then taken from the final 500 ns of the trajectory of the pre-shear-flow simulation. Using these ten configurations, ten main shear-flow simulations were performed with various shear rates for 200 ns. The ranges of the shear rate are 0.0–30.0, 0.0–15.0, 0.0–12.0, and 0.0–6.0 ns^{-1} for the S2x1, S6x1, S8x1, and S12x1 systems, respectively.

C. Velocity difference

The velocity difference between the bilayer is a measure of the intensity of the shear flow, and it is required for discussion of the bilayer stability [see Eq. (3)]. The representative x-velocity profile $u(z)$ during the final 100 ns of the 200 ns shear-flow simulation is shown in Fig. 1(b). Inside the bilayer, the x velocity was almost 0 and slightly increased with z. Outside the bilayer, the absolute value of the x velocity increased with increasing distance from the bilayer. Here, the velocity difference Δu_{MD} is defined as

$$\Delta u_{\mathrm{MD}} = \max_t \{u[z_{\max}(t)] - u[z_{\min}(t)]\}, \qquad (4)$$

where $z_{\max}(t)$ and $z_{\min}(t)$ are the maximum and minimum z coordinate of the phosphate bead of the DPPC molecules at simulation time t, respectively. The range of t is the final 100 ns of the 200 ns shear-flow simulation. Δu_{MD} represents the maximum velocity difference acting on the bilayer during the period. The velocity profile $u(z)$ in the water with the ruptured bilayers was unsteady. Thus, Δu_{MD}, where the bilayer ruptured, was not calculated from Eq. (4). It was estimated under the assumption of a linear relationship between $\dot{\gamma}$ and $|\Delta u|$ where the bilayer was not ruptured (Appendix C).

D. Bending modulus

In the MD simulation, the bending modulus of the bilayer was estimated by undulation analysis [29]. Here, l_ys of the bilayer systems was sufficiently small to suppress undulation along the y direction. Thus, as with the assumption in the linear stability analysis, we assumed uniform displacement of the bilayer along the y direction. Under the assumption of small q_x, the bending modulus k_c can be estimated by the following relationship:

$$S(q_x) = \frac{k_B T}{a(k_c q_x^4 + \sigma q_x^2)}, \qquad (5)$$

where $S(q_x)$ is the undulation spectrum of the bilayer, q_x is the wave vector in the x direction, k_B is the Boltzmann constant, T is the temperature, and a is the area per lipid. q_x is defined as $q_x = 2\pi n/l_x$ with $n = \pm 1, \pm 2, \dots$. During the equilibration simulations, the contribution of the second term (surface tension term) in the denominator of Eq. (5) was ignored as the effects were minor and did not alter the discussions and conclusions of this paper (Appendix D). Additionally, as with the assumption in the linear stability analysis, the shear-induced force and tension [14,15], which is practically
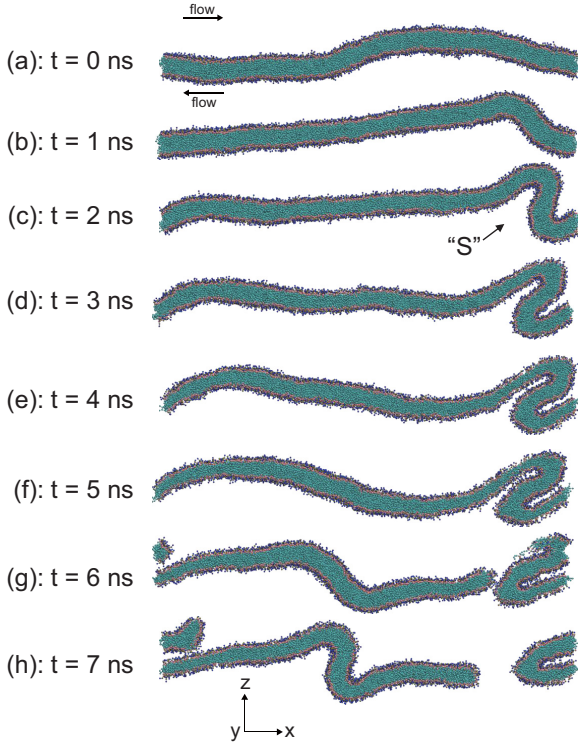
FIG. 2. Representative snapshots of the bilayer deformation process in the S12x1 system under $\dot{\gamma} = 2.0$ ns^{-1}. The bilayer deformed as an "S" shape.

FIG. 3. Representative snapshots of the bilayer deformation process in the S12x1 system under $\dot{\gamma} = 1.5$ ns^{-1}. The bilayer deformed as an "S", an "I", and an "X" shape.

difficult to evaluate in the MD simulations under shear flow, were also ignored in this paper. We fitted Eq. (5) with $\sigma = 0$ to the undulation spectra in the range $q_x < 0.7$ nm^{-1}. The average k_c for the S6x1, S8x1, and S12x1 systems was (1.62 $\pm$ 0.27) $\times$ 10^{-19} J (mean $\pm$ standard deviation), which is in good agreement with the values reported from previous simulation and experimental studies [29–31]. For this analysis, equilibration simulations were additionally performed for 2 μs.

IV. RESULTS AND DISCUSSION

A. Bilayer deformation

When the applied shear rate was below a critical level, the bilayer maintained its continuous structure with undulation during the shear-flow simulations [i.e., the stable state, Fig. 1(b)]. Conversely, above a critical level, bilayer undulation along the x direction suddenly increased, and the bilayer finally ruptured (i.e., the unstable state). As expected, remarkable undulation and/or buckling-like bilayer deformation are not observed along the y direction. We found that there were three patterns of bilayer deformation along the x direction during the rupture processes. The main deformation pattern is shown in Fig. 2 (S12x1, $\dot{\gamma} = 2.0$ ns^{-1}). Under shear flow, the bilayer locally formed a reverse "S" shape [Figs. 2(b) to 2(f)] and ruptured at the reverse-"S"-shape part [Figs. 2(g) and 2(h)]. In the S2x1, S6x1, and S8x1 systems, only this "S"-shape deformation pattern was observed. However, in the S12x1 system, different patterns appeared depending on
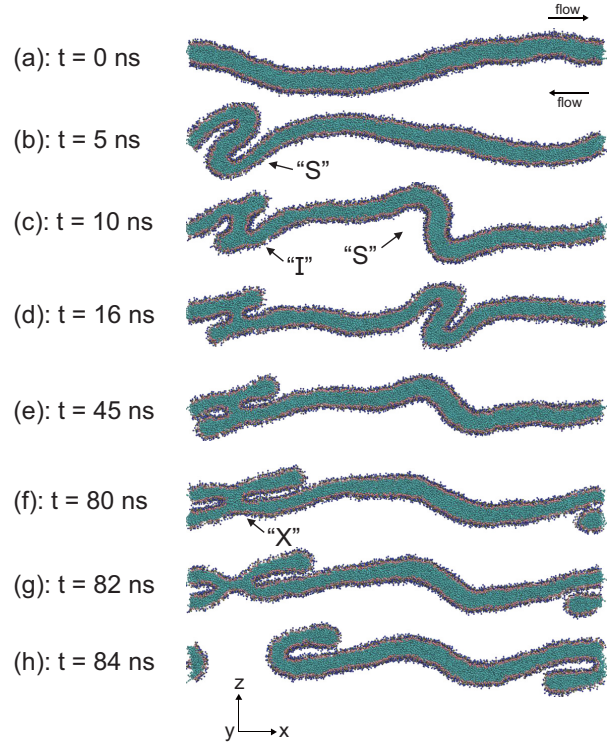
the shear rate. The second deformation pattern in the S12x1 system under $\dot{\gamma} = 1.5$ ns^{-1} is shown in Fig. 3. First, as shown in Fig. 2, an "S" shape locally formed [Fig. 3(b)]. From the bending parts of the "S" shape, the bilayer then gradually protruded and formed an "I" shape [Figs. 3(c) to 3(e)]. Furthermore, the "I" shape gradually changed into an "X" shape [Figs. 3(f) and 3(g)]. During this deformation process from an "S" shape through an "I" shape to an "X" shape, an "S" shape sometimes temporally formed in the other part of the bilayer [Figs. 3(c) and 3(d)]. The bilayer finally ruptured at the intersection of the "X" shape [Fig. 3(h)]. For the third pattern, the "I" shape formed via an "S" shape and simultaneously an additional "S" shape formed in the other part of the bilayer, as with the second pattern. The bilayer ruptured at the secondary formed "S"-shape part (see the snapshot in Fig. 4, orange).

The relationship between the shear rate and deformation patterns during the rupture process is shown in Fig. 4. The "I"- and "X"-shape deformation patterns were observed under relatively low shear rate $\dot{\gamma} \leqslant 2.0$ ns^{-1}. With increasing shear rate, the "S"-shape deformation became dominant.

The "S"-shape deformation of the bilayer under shear flow is similar to that of fluid–fluid interfaces under shear flow, which is known as the KH instability [18]. Conversely, to our knowledge, "I"- and "X"-shape deformations under shear flow have not been previously reported. Similar deformation patterns of the bilayer were proposed as energetically reasonable pathways for processes in which two lipid vesicles fuse
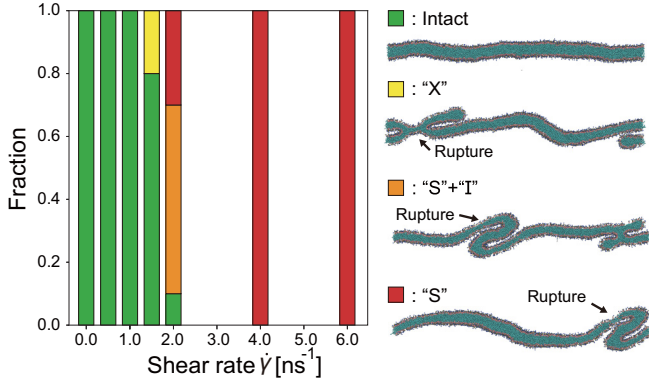
FIG. 4. Stacked bar chart of fractions of the deformation patterns during the rupture processes observed in the S12x1 system. The fraction of intact, rupture at the "X" shape part, "S" shape part with "I" shape, and "S" shape part are shown in green, yellow, orange, and red, respectively. The representative snapshots of the bilayer deformation patterns are also shown. The arrows point to the parts where the bilayer ruptured.

into one (membrane fusion) or one vesicle divides into two (membrane division) [32–34]. Because of the similarity in the bilayer deformation pattern, the shear-induced "I"- and "X"- shape deformations might become energetically favorable in the lower range of the shear rate.

B. Critical shear rate and velocity difference

The bilayer became unstable (i.e., ruptured) depending on the shear rate. To quantify the critical shear rate for instability, we calculated the probability of instability-induced bilayer rupture P as a function of $\dot{\gamma}$ (Fig. 5). P is defined as $P = N_i/N_t$, where N_i is the number of trials of bilayer rupture during the shear-flow simulations and N_t is the total number of trials ($N_t = 10$). P was fitted by $\{1 + \mathrm{erf}[(\dot{\gamma} - \bar{\dot{\gamma}}_c)/\sqrt{2}s]\}/2$, where erf is the error function, $\bar{\dot{\gamma}}_c$ and s are the mean and standard deviation of the critical shear rate $\dot{\gamma}_c$, respectively (see Fig. 5). With increasing $\dot{\gamma}$, P monotonically increased
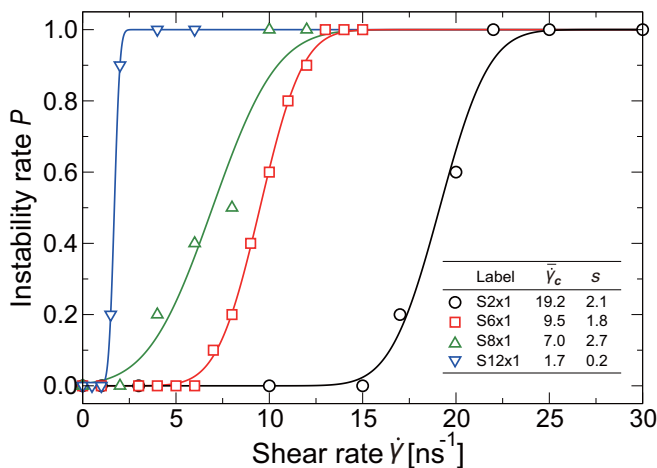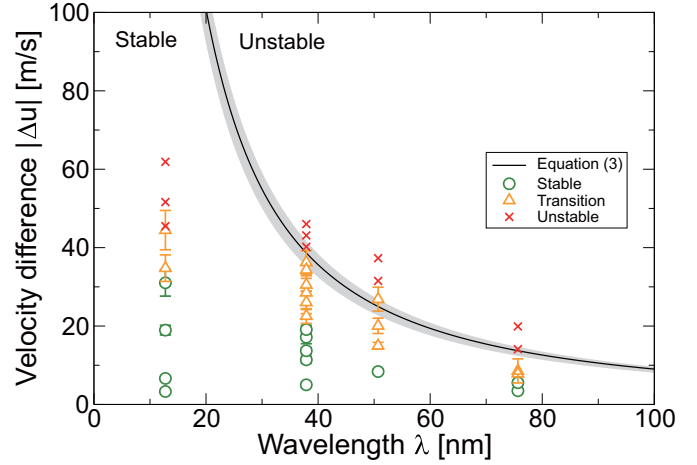

FIG. 6. Relationship between the wavelength of bilayer undulation λ and the velocity difference across the bilayer Δu. The symbols are the results obtained in the MD simulations. Green circles, orange triangles, and red crosses represent the stable, transition, and unstable phases, respectively. The error bars represent the standard deviation. The solid lines show the critical velocity difference Δu_c calculated from Eq. (3) with the average k_c. The region between Δu_c with average k_c plus and minus the standard deviation is shown in gray. The lower left side and the upper right side of the solid line correspond to the stable and the unstable regions predicted from Eq. (3), respectively.

and reached 1.0. The curve shifted to lower shear rate with increasing system size. The data were successfully fitted by the above fitting function. $\bar{\dot{\gamma}}_c$ decreased with increasing system size.

Equation (3) predicts the critical velocity difference Δu_c, where the bilayer becomes unstable, as a function of the wavelength λ. To adjust the explanatory variable for the bilayer stability in the MD simulation to that in the model (Δu and λ), we defined that Δu_{MD} is calculated based on Eq. (4) with applied $\dot{\gamma}$ and λ is equal to the simulation box length in the x direction l_x. The relationship between Δu_{MD} and λ for each $\dot{\gamma}$ is shown in Fig. 6. In Fig. 6, the points are plotted as three different symbols depending on the phase of the bilayer stability: the stable phase when $P(\dot{\gamma}) = 0$, the unstable phase when $P(\dot{\gamma}) = 1$, and the transition phase in the other cases. In the transition phases, Δu_{MD} decreased with increasing λ.

C. Bilayer stability

We compared the stabilities of the bilayer under shear flow obtained from the MD simulations and predicted by the theoretical model. Δu_c for the model is plotted on the $|\Delta u|$–λ diagram (Fig. 6). To obtain Δu_c, ρ was calculated to be $986 \, \mathrm{kg/m^3}$ from a MD simulation of the bulk water system. Δu_c for the model decreased with increasing λ, as with Δu for the transition phases of the MD simulations. Δu_c was in good agreement with Δu for the transition phases, except for the S2x1 system ($\lambda = 12.8 \, \mathrm{nm}$). For the S2x1 system, the theoretical prediction overestimated $|\Delta u_c|$ compared with that in the MD simulation.

Label	$\bar{\bar{\gamma}}_c$	s
S2x1	19.2	2.1
S6x1	9.5	1.8
S8x1	7.0	2.7
S12x1	1.7	0.2

FIG. 5. Relationship between the applied shear rate $\dot{\gamma}$ and the instability rate P.

For larger λ ($>$ about 30 nm), the simple macroscopic stability model was applicable for the shear-induced KH-like instability of the bilayer. The model showed that the critical velocity difference across the bilayer was proportional to the length of the simulation box along the flow direction to the power of $-3/2$ [see Eq. (3)]. According to this scaling law, the critical velocity difference at the cell scale ($\sim$1–10 μm) was estimated to be about 0.01–0.1 m/s. Dividing this by the bilayer thickness, the shear rate across the bilayer was estimated to be about 10^6–10^7 s^{-1}. It is noted that considering the ignored factors, e.g., the shear-induced tension, into the theoretical model might improve the estimation of the critical shear rate for larger λ.

Experimental researchers investigated various phases of bilayer membranes, including biological cells, under shear flow. For a lamellar phase of bilayer membranes, a transition to a multilamellar vesicle phase (an onion formation) occurs under shear rate of 1–10^2 s^{-1} [13,35,36]. Structurally, the transition from the lamellar phase to the multilamellar vesicle phase must include the membrane rupture. For biological cells, cell lysis, which is considered to be caused by membrane rupture, occurs under shear rate of $>10^3$ s^{-1} [37–40]. It has also been reported that lipid bilayer vesicles can withstand shear rate of $\sim10^4$ s^{-1} without leaking of their contents [41]. From these results, we deduced that such membrane rupture under shear flow is not usually caused by KH-like instability, but it is caused by other mechanisms, such as buckling-like instability [14,15] or cell elongation [42].

In the case of medical treatment, jet injection devices shoot drug solutions into the tissues, where the initial jet velocity is $\sim10^2$ m/s and the orifice diameter is $\sim10^{-4}$ m [43,44]. Additionally, some types of rheometers can induce much higher shear flow ($\dot{\gamma} \sim 10^7$ s^{-1}) [45] than the rheometers used in studies of biological cells and lipid bilayer vesicles ($<10^5$ s^{-1}) [37–41]. In such drastic cases, the shear rate might reach the theoretically predicted critical value, although it is now difficult to predict the local shear rate near the cells experimentally or numerically.

For smaller λ ($<$ about 30 nm), the theoretical model overestimated the critical value of the bilayer instability in the MD simulation (Fig. 6). This discrepancy might be because of the limitations of the Helfrich Hamiltonian used in the model. As mentioned in Sec. II, the Helfrich Hamiltonian assumes that the bilayer is sufficiently thin compared with the lengthscale, and it is less accurate when this assumption is not valid. Kawamoto and co-workers [20] performed MD simulations of the bilayer to estimate the bilayer bending modulus based on the Helfrich Hamiltonian. They found that the estimated bending modulus is smaller when the system size is smaller than about ten times the thickness of the hydrophobic part of the bilayer. This indicates that the simple Helfrich-based model may overestimate the bilayer rigidity for the bending in the smaller system (i.e., the S2x1 system). This might be a reason for the higher critical velocity difference in the model (Fig. 6). Formulating the bending energy in a small system is usually difficult, but it has been addressed, such as by introducing curvature-dependent elastic parameters [46]. Extending the model for the bilayer stability in combination with such a method will improve our understanding of the instability at smaller λ.
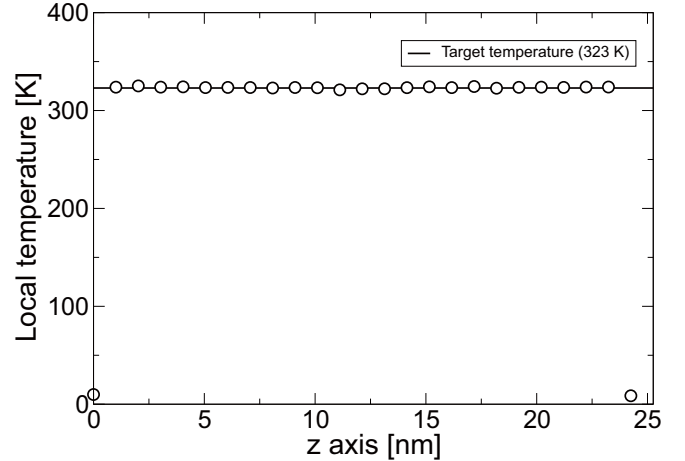

FIG. 7. Representative local temperatures in the bins along the z axis in the S2x1 system with $\dot{\gamma} = 10.0$ ns^{-1}. The local temperatures are shown by open circles and the target temperature of 323 K is shown by the line.

V. CONCLUSION

In this study, we estimated the effect of the system size on the shear-induced KH-like instability of phospholipid bilayers by MD simulations and extended it by using the framework of linear stability analysis. In the MD simulations, the critical velocity difference across the bilayer, where instability occurs, decreased with increasing system size. This tendency is in quantitative agreement with the theoretical prediction, which is valid when the wavelength of the bilayer is more than about ten times larger than the bilayer thickness. By the combination of MD simulation and the theoretical model, the critical velocity difference was estimated to be proportional to the system size along the flow direction to the power of $-3/2$. Based on the model, we deduced that the shear-induced cell damage observed in experiments is usually not caused by KH-like instability. The model also predicted that the high shear flow situation, in which the shear rate is $\sim10^6$ s^{-1}, might induce KH-like instability of the bilayer.

APPENDIX A: VERIFICATION OF LOCAL TEMPERATURE CONTROL

Representative local temperatures in the bins along the z axis in the S2x1 system with $\dot{\gamma} = 10.0$ ns are shown in Fig. 7. Except for the slab of the wall particles ($z = 0$ and 24–25 nm), the local temperatures agreed with the target temperature (323 K).
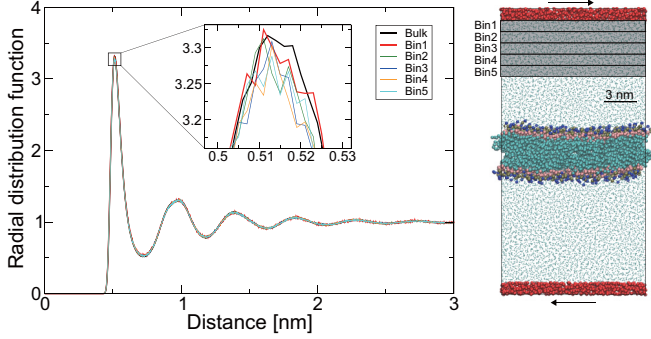
FIG. 8. (Left) Representative local RDFs in 1.0-nm-bins along z axis in the S2x1 system under $\dot{\gamma} = 20.0$ ns^{-1}. RDF for bulk water system under $\dot{\gamma} = 0.0$ ns^{-1} is also shown in the left panel (black line). (Right) A representative snapshot of the S2x1 system under $\dot{\gamma} = 20.0$ ns^{-1}. 1.0-nm bins used for the calculation of the local radical distribution functions are shown in gray.

APPENDIX B: EFFECTS OF LOCAL TEMPERATURE CONTROL ON THE LOCAL STRUCTURE OF WATER

Representative local radial distribution functions (RDFs) in 1.0-nm bins along the z axis in the S2x1 system under $\dot{\gamma} = 20.0$ ns^{-1} are shown in Fig. 8. The local RDFs did not depend on the position of the bin and agreed with the RDF for bulk water without shear flow. This indicated that the local temperature control here did not artificially alter the local radial distribution of water particles and reproduced the characteristics of the bulk water even near the wall.

APPENDIX C: RELATIONSHIP BETWEEN THE SHEAR RATE AND THE VELOCITY DIFFERENCE

The relationships between the applied shear rate $\dot{\gamma}$ and velocity difference Δu_{MD} are shown in Fig. 9. For all of the systems, Δu_{MD} almost linearly increased with increasing $\dot{\gamma}$. Although the plots for the larger systems (S6x1, S8x1, and S12x1) were almost on the same straight line (solid line), that for the smallest system S2x1 was on a different line (dashed line). The solid line in Fig. 9 was a fitting line for the S6x1, S8x1, and S12x1 systems by the linear squares method, and the dashed line was that for the S2x1 system. In the S2x1 system, the undulation of the bilayer was strongly suppressed by the small system size. This decreased the maximum amplitude of undulation, resulting in smaller Δu compared to those in the other systems. Based on these two linear relations, Δu_{MD} in the case where the bilayer ruptured was estimated from the applied shear rate $\dot{\gamma}$.

APPENDIX D: EFFECTS OF SURFACE TENSION

In this study, we ignored the surface tension σ in Eq. (5). However, when the wavelength of the undulation λ is larger than a crossover wavelength $\lambda_c(\sigma, k_c) = 2\pi/|\sigma/k_c|^{1/2}$, the surface tension term becomes dominant and is not ignorable in Eq. (5). To justify this, we calculated λ_c and a contribution ratio $R_s(\sigma, k_c) = 4\pi^2(\sigma/k_c)l_x^{-2}$, representing the ratio of the surface tension term to the bending rigidity term in Eq. (5). To
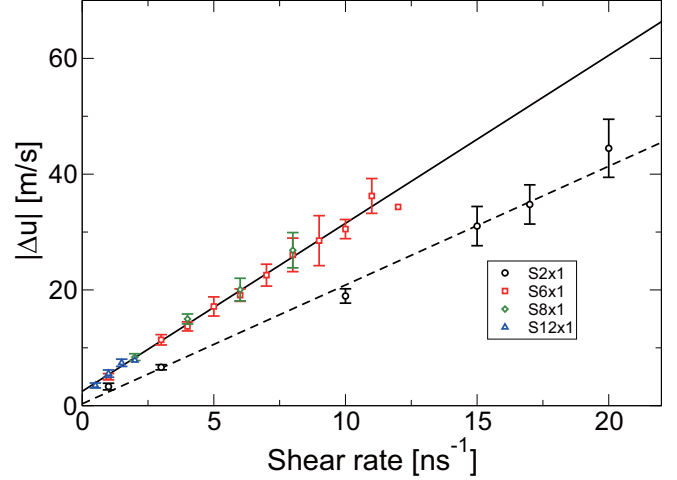

FIG. 9. Relationship between the applied shear rate $\dot{\gamma}$ and the velocity difference across the bilayer Δu. The error bars represent the standard deviation.

calculate λ_c and R_s, we first computed the surface tension σ as the surface tension in the equilibrium simulations, denoted as $\sigma_{\mathrm{eq}} = (2P_{zz} - P_{xx} - P_{yy})l_z/2$, where P_{ii} is a component of the pressure tensor ($i = x, y, z$). As with k_c with the assumption of the zero surface tension, k_c with $\sigma = \sigma_{\mathrm{eq}}$ was estimated by fitting Eq. (5) with $\sigma = \sigma_{\mathrm{eq}}$ to undulation spectrum in the range of $q_x < 0.7$ nm^{-1} and denoted as $k_c^{\sigma\mathrm{eq}}$.

These values for all the systems are summarized in Table I. $\lambda_c(\sigma_{\mathrm{eq}}, k_c)$ and $\lambda_c(\sigma_{\mathrm{eq}}, k_c^{\sigma\mathrm{eq}})$ were larger than the system size l_x. Additionally, $R_s(\sigma_{\mathrm{eq}}, k_c)$ and $R_s(\sigma_{\mathrm{eq}}, k_c^{\sigma\mathrm{eq}})$ were at most 17% (for the S6x1 system). These mean that the effects of the bending rigidity were greater than those of the surface tension. Such the differences between including and excluding the surface tension did not alter the discussions and conclusions of this paper.

TABLE I. Parameters related to the balance between the surface tension and the bending rigidity

Label	S2x1	S6x1	S8x1	S12x1
σ_{eq} [mN/m]	-1.51	0.52	0.08	0.03
k_c [$\times10^{-19}$ J]	2.24[a]	1.32	1.83	1.72
$k_c^{\sigma\mathrm{eq}}$ [$\times10^{-19}$ J]	2.30[a]	1.13	1.77	1.67
l_x [nm]	12.8	37.9	50.7	75.7
$\lambda_c(\sigma_{\mathrm{eq}}, k_c)$ [nm]	76.4	100	300	464
$\lambda_c(\sigma_{\mathrm{eq}}, k_c^{\sigma\mathrm{eq}})$ [nm]	77.5	92.7	295	457
$R_s(\sigma_{\mathrm{eq}}, k_c)$ [-]	-0.03	0.14	0.03	0.03
$R_s(\sigma_{\mathrm{eq}}, k_c^{\sigma\mathrm{eq}})$ [-]	-0.03	0.17	0.03	0.03

[a]Fitted in the range $q_x < 1.0$ nm^{-1} because the usual range ($q_x < 0.7$ nm^{-1}) was too small for the fitting in the S2x1 system [$q_x(n = 1) = 0.49$ nm^{-1} and $q_x(n = 2) = 0.99$ nm^{-1}].

[1] A. M. Malek and S. Izumo, Mechanism of endothelial cell shape change and cytoskeletal remodeling in response to fluid shear stress, J. Cell Sci. **109**, 713 (1996).

[2] S. Chien, S. Li, and J. Y-J. Shyy, effects of mechanical forces on signal transduction and gene expression in endothelial cells, Hypertension **31**, 162 (1998).

[3] U. A. Gurkan and O. Akkus, The mechanical environment of bone marrow: A review, Ann. Biomed. Eng. **36**, 1978 (2008).

[4] S. Deutsch, J. M. Tarbell, K. B. Manning, G. Rosenberg, and A. A. Fontaine, Experimental fluid mechanics of pulsatile artificial blood pumps, Annu. Rev. Fluid Mech. **38**, 65 (2006).

[5] J. H. Chang, N. C. Hogan, and I. W. Hunter, A needle-free technique for interstitial fuid sample acquisition using a lorentz-force actuated jet injector, J. Controlled Release **211**, 37 (2015).

[6] D. L. Miller, S. V. Pislaru, and J. E. Greenleaf, Sonoporation: mechanical DNA delivery by ultrasonic cavitation., Somatic Cell Mol. Genet. **27**, 115 (2002).

[7] A. Delalande, S. Kotopoulis, M. Postema, P. Midoux, and C. Pichon, Sonoporation: mechanistic insights and ongoing challenges for gene transfer, Gene **525**, 191 (2013).

[8] L. Leverett, L. Hellums, C. Alfrey, and E. Lynch, Red blood cell damage by shear stress, Biophys. J. **12**, 257 (1972).

[9] P. Marmottant, T. Biben, and S. Hilgenfeldt, Deformation and rupture of lipid vesicles in the strong shear flow generated by ultrasound-driven microbubbles, Proc. R. Soc. A **464**, 1781 (2008).

[10] T. Omori, T. Ishikawa, Y. Imai, and T. Yamaguchi, Membrane tension of red blood cells pairwisely interacting in simple shear flow, Journal of Biomechanics **46**, 548 (2013).

[11] I. Hanasaki, J. H. Walther, S. Kawano, and P. Koumoutsakos, Coarse-grained molecular dynamics simulations of shear-induced instabilities of lipid bilayer membranes in water, Phys. Rev. E **82**, 051602 (2010).

[12] S. Ramaswamy, Shear-Induced Collapse of the Dilute Lamellar Phase, Phys. Rev. Lett. **69**, 112 (1992).

[13] O. Diat, D. Roux, and F. Nallet, Effect of shear on a lyotropic lamellar phase, J. Phys. II **3**, 1427 (1993).

[14] A. Zilman and R. Granek, Undulation instability of lamellar phases under shear: A mechanism for onion formation?, Eur. Phys. J. B **11**, 593 (1999).

[15] S. W. Marlow and P. D. Olmsted, The effect of shear flow on the Helfrich interaction in lyotropic lamellar systems, Eur. Phys. J. E **8**, 485 (2002).

[16] T. V. Tolpekina, W. K. den Otter, and W. J. Briels, Simulations of stable pores in membranes: System size dependence and line tension., J. Chem. Phys. **121**, 8014 (2004).

[17] T. Shigematsu, K. Koshiyama, and S. Wada, Stretch-induced interdigitation of a phospholipid/cholesterol bilayer, J. Phys. Chem. B **122**, 2556 (2018).

[18] F. Charru, *Hydrodynamic Instabilities*, edited by P. de Forcrand-Millard, Cambridge Texts in Applied Mathematics (Cambridge University Press, Cambridge, England, 2011).

[19] W. Helfrich, Elastic properties of lipid bilayers: theory and possible experiments, Z. Naturforschung C **28**, 693 (1973).

[20] S. Kawamoto, T. Nakamura, S. O. Nielsen, and W. Shinoda, A guiding potential method for evaluating the bending rigidity of tensionless lipid membranes from molecular simulation, J. Chem. Phys. **139**, 034108 (2013).

[21] S. Komura and T. Iwayama, Kelvin-helmholtz instability of langmuir monolayers, Journal de Physique II **7**, 1331 (1997).

[22] S. J. Marrink, H. J. Risselada, S. Yefimov, D. P. Tieleman, and A. H. de Vries, The MARTINI force field: coarse grained model for biomolecular simulations., J. Phys. Chem. B **111**, 7812 (2007).

[23] Y. Qi, H. I. Ingólfsson, X. Cheng, J. Lee, S. J. Marrink, and W. Im, CHARMM-GUI Martini Maker for Coarse-Grained Simulations with the Martini Force Field, J. Chem. Theory Comput. **11**, 4486 (2015).

[24] D. H. De Jong, S. Baoukina, H. I. Ingólfsson, and S. J. Marrink, Martini straight: Boosting performance using a shorter cutoff and GPUs, Comput. Phys. Commun. **199**, 1 (2016).

[25] H. J. C. Berendsen, J. P. M. Postma, W. F. van Gunsteren, A. DiNola, and J. R. Haak, Molecular dynamics with coupling to an external bath, J. Chem. Phys. **81**, 3684 (1984).

[26] H. Berendsen, D. van del Spoel, and R. van Drunen, GRO-MACS: A message-passing parallel molecular dynamics implementation, Comput. Phys. Commun. **91**, 43 (1995).

[27] B. Hess and C. Kutzner, GROMACS 4: Algorithms for highly efficient, load-balanced, and scalable molecular simulation, J. Chem. Theory Comput. **4**, 435 (2008).

[28] W. Humphrey, A. Dalke, and K. Schulten, VMD: Visual molecular dynamics, J. Mol. Graphics **14**, 33 (1996).

[29] E. G. Brandt, A. R. Braun, J. N. Sachs, J. F. Nagle, and O. Edholm, Interpretation of fluctuation spectra in lipid bilayer simulations, Biophys. J. **100**, 2104 (2011).

[30] A. K. Chaurasia, A. M. Rukangu, M. K. Philen, G. D. Seidel, and E. C. Freeman, Evaluation of bending modulus of lipid bilayers using undulation and orientation analysis, Phys. Rev. E **97**, 032421 (2018).

[31] K. Koshiyama, M. Taneo, T. Shigematsu, and S. Wada, Bicelle-to-vesicle transition of a binary phospholipid mixture guided by controlled local lipid compositions: A molecular dynamics simulation study, J. Phys. Chem. B **123**, 3118 (2019).

[32] L. V. Chernomordik and M. M. Kozlov, Mechanics of membrane fusion, Nat. Struct. Mol. Biol. **15**, 675 (2008).

[33] S. Kawamoto and W. Shinoda, Free energy analysis along the stalk mechanism of membrane fusion, Soft Matter **10**, 3048 (2014).

[34] T. Salditt and S. Aeffner, X-ray structural investigations of fusion intermediates: Lipid model systems and beyond, Seminars Cell Developmental Biology **60**, 65 (2016).

[35] D. Sato, K. Obara, Y. Kawabata, M. Iwahashi, and T. Kato, Re-entrant lamellar/onion transition with varying temperature under shear flow, Langmuir **29**, 121 (2013).

[36] T. Kato, *Advances in Biomembranes and Lipid Self-Assembly*, 1st ed., Vol. 27, (Elsevier, New York, 2018), pp. 187–222.

[37] C. G. Smith, P. F. Greenfield, and D. H. Randerson, A technique for determining the shear sensitivity of mammalian cells in suspension culture, Biotechnol. Tech. **1**, 39 (1987).

[38] I. Abu-Reesh and F. Kargi, Biological responses of hybridoma cells to defined hydrodynamic shear stress, J. Biotechnol. **9**, 167 (1989).

[39] J. F. Petersen, L. V. McIntire, and E. T. Papoutsakis, Shear sensitivity of cultured hybridoma cells (CRL-8018) depends on mode of growth, culture age and metabolite concentration, J. Biotechnol. **7**, 229 (1988).

[40] T. Tanzeglock, M. Soos, G. Stephanopoulos, and M. Morbidelli, Induction of mammalian cell death by simple shear and extensional flows, Biotechnol. Bioeng. **104**, 360 (2009).

[41] Ž. Pandur, I. Dogsa, M. Dular, and D. Stopar, Liposome destruction by hydrodynamic cavitation in comparison to chemical, physical and mechanical treatments, Ultrasonics Sonochemistry **61**, 104826 (2020).

[42] S. Sohrabi and Y. Liu, A cellular model of shear-induced hemolysis, Artificial Organs **41**, E80 (2017).

[43] P. Rohilla, Y. S. Rane, I. Lawal, A. Le Blanc, J. Davis, J. B. Thomas, C. Weeks, W. Tran, P. Fisher, K. E. Broderick, J. A. Simmons, and J. O. Marston, Characterization of jets for impulsively-started needle-free jet injectors: Influence of fluid properties, J. Drug Delivery Sci. Technol. **53**, 101167 (2019).

[44] H. Miyazaki, S. Atobe, T. Suzuki, H. Iga, and K. Terai, Development of pyro-drive jet injector with controllable jet pressure, J. Pharm. Sci. **108**, 2415 (2019).

[45] T. T. Dao, A. X. Ye, A. A. Shaito, N. Roye, and K. Hedman, Capillary rheometry: Analysis of low-viscosity fluids, and viscous liquids and melts at high shear rates, Amer. Lab. **41**, 14 (2009).

[46] T. Nakamura and W. Shinoda, Method of evaluating curvature-dependent elastic parameters for small unilamellar vesicles using molecular dynamics trajectory, J. Chem. Phys. **138**, 124903 (2013).